2014

The influence of an Antarctic glacier tongue on near-field ocean circulation and mixing

Stevens, C.L.

AGU Publications

AGU PUBLICATIONS

JGR

Journal of Geophysical Research: Oceans

RESEARCH ARTICLE

10.1002/2013JC009070

Key Points:
- A blocking layer is generated by the floating glacier
- Tidal rectification or substantial residual flow results in tidal asymmetry
- Upper water column mixing is at least as strong during neap tides as spring

Correspondence to:
C. L. Stevens,
c.stevens@niwa.cri.nz

Citation:
Stevens, C. L., M. G. McPhee, A. L. Forrest, G. H. Leonard, T. Stanton, and T. G. Haskell (2014), The influence of an Antarctic glacier tongue on near-field ocean circulation and mixing, *J. Geophys. Res. Oceans*, *119*, 2344–2362, doi:10.1002/2013JC009070.

Received 30 APR 2013
Accepted 17 MAR 2014
Accepted article online 24 MAR 2014
Published online 14 APR 2014

The influence of an Antarctic glacier tongue on near-field ocean circulation and mixing

C. L. Stevens[1,2], M. G. McPhee[3], A. L. Forrest[4,5], G. H. Leonard[6], T. Stanton[7], and T. G. Haskell[8]

[1]Marine Physics, National Institute of Water and Atmospheric Research, Greta Point, Wellington, New Zealand, [2]Physics Department, University of Auckland, Auckland, New Zealand, [3]McPhee Research Company, Naches, Washington, USA, [4]Australian Maritime College, University of Tasmania, Launceston, Tasmania, Australia, [5]Tahoe Environmental Research Center, University of California Davis, Davis, California, USA, [6]School of Surveying, University of Otago, Dunedin, New Zealand, [7]Naval Postgraduate School, Monterey, California, USA, [8]Industrial Research Ltd., Lower Hutt, New Zealand

Abstract In situ measurements of flow and stratification in the vicinity of the Erebus Glacier Tongue, a 12 km long floating Antarctic glacier, show the significant influence of the glacier. Three ADCPs (75, 300, and 600 kHz) were deployed close (<50 m) to the sidewall of the glacier in order to capture near-field flow distortion. Scalar (temperature and conductivity) and shear microstructure profiling captured small-scale vertical variability. Flow magnitudes exceeded 0.3 m s^{-1} through a combination of tidal flow (~8 cm s^{-1}) and a background/residual flow (~4–10 cm s^{-1}) flowing to the NW. Turbulence was dominated by deeper mixing during spring tide, likely indicative of the role of bathymetric variation which locally forms an obstacle as great as the glacier. During the neap tide, near-surface mixing was as energetic as that seen in the spring tide, suggesting the presence of buoyancy-driven near-surface flows. Estimates of integrated dissipation rate suggest that these floating extensions of the Antarctic ice sheet alter energy budgets through enhanced dissipation, and thus influence coastal near-surface circulation.

1. Introduction

Glacier tongues, the seaward extension of glacier outflows, form substantial obstacles along the coastal margins of Antarctica. For example, along the coastline of Victoria Land on the western margin of the Ross Sea there are at least 10 substantial glacier tongues (Nordenskjöld, Harbord, Cheetham, Campbell, Drygalski, Tinker, Aviator, Icebreaker, Mariner, and Borchgrevink [*Gunn and Warren*, 1962; *Debenham*, 1965; *Frezzotti*, 1997]; Figure 1a). With offshore extensions into the coastal ocean of 10 km or more, and vertical thicknesses of 100–300 m, they likely significantly modify coastal surface currents as well as constrict flow between the coast and offshore islands (e.g., Coulman Glacier and the Kay Islands). Thus, there is interest in the connection between these glacial outflows and Antarctic regional coastal circulation [*Moffat et al*., 2008; *Hellmer et al*., 2012; K. Hughes et al., Extension of an ice shelf water plume model beneath sea ice, submitted to *Journal of Geophysics Research*-Oceans, 2013].

In this work, we use detailed observations of flow and stratification near the Erebus Glacier Tongue (hereinafter EGT), a small glacier tongue in southern McMurdo Sound, to quantify likely effects on stratification and coastal currents resulting from such obstacles. The provenance and fate of coastal currents are particularly important at high southern latitudes due to the advection of near-surface layers of ice shelf water [*Mahoney et al*., 2011]. The water in these layers has been in contact with the underside of ice shelves at significant depths where it cooled to the melting temperature at that pressure. The melting introduces freshwater [*Holland and Jenkins*, 1999] and the resulting reduced density drives flow to shallower depths. The associated reduction in pressure raises the temperature of freezing, resulting in the still-liquid seawater being colder than its local freezing point. This thermal deficit is not instantly relieved by freezing and so the seawater is said to be supercooled. *Mahoney et al*. [2011] show layers of this fluid being present at a location a few km south of the EGT at a number of times during their year-long sampling.

Supercooled water dramatically affects both the nature of sea ice and its propensity to form crystals [*Smith et al*., 2001; *Dmitrenko et al*., 2010; *Gough et al*., 2012]. *Stevens et al*. [2009] and K. Hughes et al. (submitted manuscript, 2013) used diffusive arguments and a plume model, respectively, to suggest that the flow of supercooled water from the combined McMurdo and Ross Ice Shelves to the south of McMurdo Sound through Haskell Strait (south of Cape Armitage and Scott Base, Figure 1c), might persist northward for as

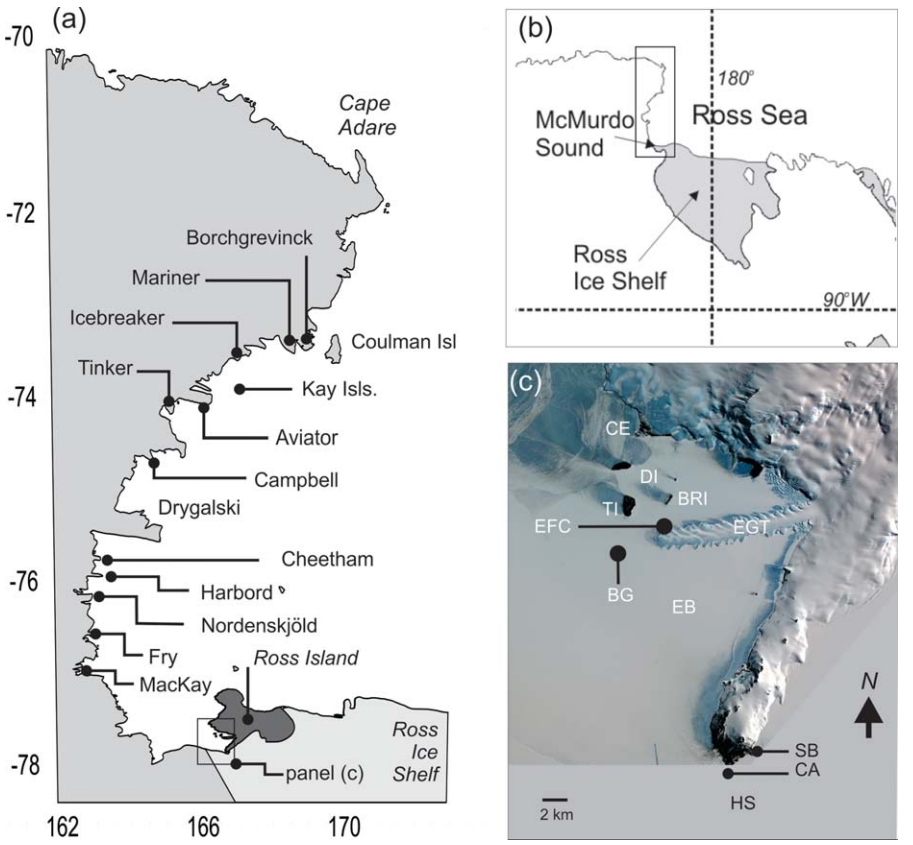

Figure 1. (a) Regional map of Victoria Land coast with locations of glacier tongues with insets showing (b) location of Figure 1a within Antarctica and (c) ASTER (Advanced Space borne Thermal Emission and Reflection Radiometer) satellite image of south east McMurdo Sound including the Erebus Glacier Tongue (EGT), the Dellbridge Islands (DI), Erebus Bay (EB), Cape Evans (CE), Cape Armitage (CA), Haskell Strait (HS), Scott Base (SB), background mooring (BG), and the Erebus Field Camp (EFC). The Dellbridge Islands include Tent Island (TI) and Big Razorback Island (BRI).

much as 250 km before being diluted through mixing. Even once this layer warms above the local freezing temperature, it will still aid atmospherically driven sea ice formation as the stratification will restrict the vertical extent of heat loss.

The EGT divides the surface waters of Erebus Bay between the Dellbridge Islands and Cape Armitage (Figure 1). The present work builds on a brief pilot study conducted in 2009 in the same location [*Stevens et al.*, 2011]. Observations of flow speeds of 40 cm s^{-1} were made during this study and conditions suitable for shear-generated turbulence were identified. The present work extends the duration of the sampling by a factor of three compared to the pilot study, enabling comparison of spring and neap phases of the tide. Furthermore, the depth range of the observations is nearly tripled whilst the spatial perspective is expanded through the use of multiple field stations. Associated work includes analysis of the underice boundary layer variability in supercooling conditions, acoustic backscatter from ADCPs under the influence of ice shelf water, and the horizontal scalar structure of the wake region as measured with an autonomous underwater vehicle.

The questions we seek to answer here are: (i) what is the character of the flow disturbance caused by the glacier? (ii) to what levels are local mixing rates elevated and do these rates include a signature associated with the spring-neap cycle? and (iii) what are the implications of these high-resolution near-wall results for glacier melting rate estimates?

2. Methods

2.1. Location

At the time of sampling, the glacier tongue was 12 km long, 1.5 km wide, and was estimated to be 300 m thick at the grounding line. The basal slope was ~0.02 along its main axis, and the tip was ~50 m thick (Figure 2) [*DeLisle et al.*, 1989]. The tip was almost at the longitude of Tent Island (Figure 2a).

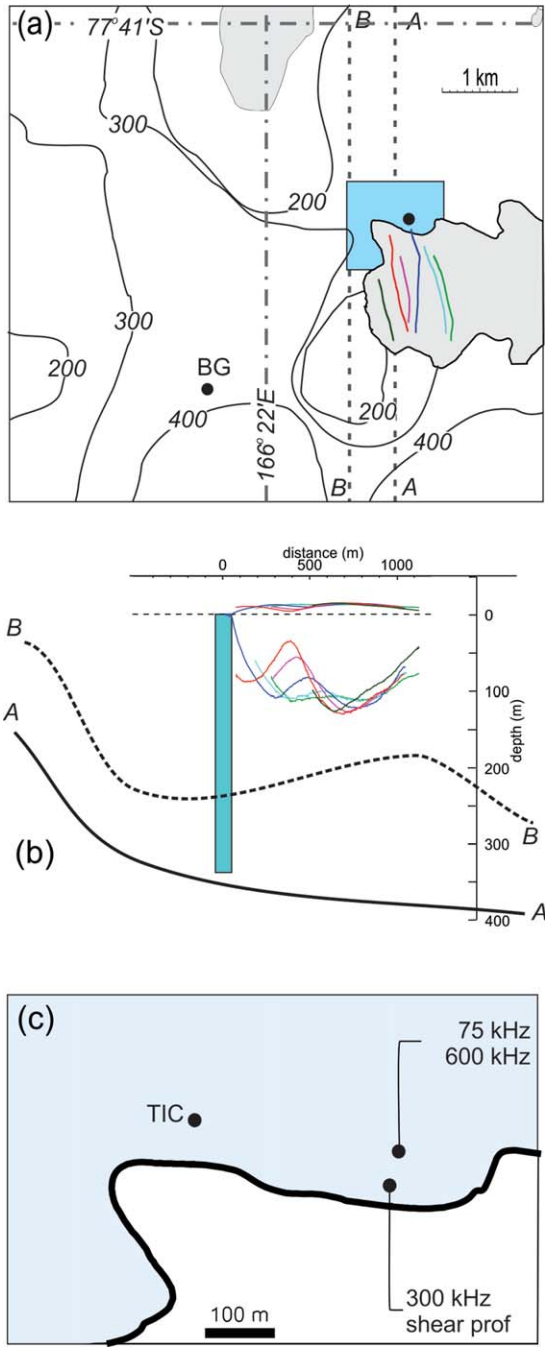

Figure 2. GPS survey showing (a) a plan view of the outline of EGT and local bathymetry with a number of freeboard transects that correspond to the (b) elevation view where glacier depth is computed from GPS assuming an ice density of 867 kg m^{-3}. The approximate bathymetry in Figure 2b is at the A-A and B-B longitudes shown in Figure 2a. The green box shows the location of profiling. (c) The arrangement of the Erebus Field Camp (EFC) includes the three acoustic profilers (75, 300, and 600 kHz), shear microstructure profiler, and the turbulence instrumentation cluster stations (TIC).

With the variability in glacier position, all references relative to the tip location are for the October 2010 position. As well as the tip moving at 100–200 m/yr, there are periodic calving events. At the time of the sampling, the most recent calving of the EGT had been in March 1990 when a 3.5 km section broke away [*Robinson and Haskell*, 1990]. Subsequent to the observations described here, a 4 km section calved off in February 2013 [*Stevens et al*., 2013]. Similar events were known to have occurred in 1911 and at some point during the 1940s [*Holdsworth*, 1982].

The few bathymetric data available in the area are collated in Land Information New Zealand chart NZ14901 and show there are no bathymetric data to the east of Big Razorback Island (Figure 1c). The water depth near the EGT tip was around 400 m when the sampling described in *Jacobs et al*. [1981] took place. However, the "depth at the tip" is variable due to the changing position of the glacier tip and the complex geography of the region (Figure 2), most notably the region shoaling to 190 m, just to the west of the October 2010 tip position.

The above-water glacier outline was traced with skidoo-mounted Global Positioning System (GPS), and in some areas by ski. This enabled the face of the glacier to be mapped within a few m (Figure 2). A field camp (Erebus Field Camp—EFC) was established off the NW tip of the EGT using modified insulated shipping containers; with those being used for sampling having hatches in the floor to access the ice. Hydroholes were then created with a hot water drill designed to generate wide (~1 m diameter) holes in thin sea ice. At the location of the EFC, the ice was first year sea ice with a uniform thickness of ~2.3 m. An initial subsurface survey with a remotely operated vehicle (ROV) showed that the first year sea ice underside was reasonably homogeneous and no ice rafting was apparent in the region.

Despite the EFC being close to the tip, the proximity to the glacier sidewall meant that we were sampling sidewall rather than "tip" effects. If the camp had been much closer to the Ross Island coast there would have been significant challenges accessing the water as the result of the thickness of both the sea ice and the glacier. The measured water depth at the EFC site was 344 m using an acoustic sounder and so substantially deeper than the shoaling region to the west of the tip.

Table 1. ADCP Deployments

Unit (kHz)	600	300	75
Location	−77°42.145′ 166°26.778′	−77°42.179′ 166°26.741′	−77°42.145′ 166°26.778′
Bin size (m)	0.5	2	8
Center first bin (m)	3.25	5.4	14.5
Typical maximum depth (m)	35	80	300
Averaging/sampling time step (min)	10	2	2

Glacier freeboard was measured with several precise GPS elevation transects across the top of the EGT conducted 2 weeks after the oceanographic work. These transects used a Trimble R7 receiver tied to regional GPS base stations (located approximately 18 km from the experiment site) and produced 3-D positions with horizontal and vertical accuracies of approximately 1 and 3 cm, respectively. Estimates of the ice thickness can then be determined from hydrostatics assuming that the glacier density is 867 kg m^{-3} [*Holdsworth*, 1974] and that the firn covering on the EGT played a relatively minor role as it was a few centimeter at most (e.g., comparable to the accuracy of the GPS) due to the substantial ablation (S. Mager, personal communication, 2013).

2.2. Tides and Background Mooring

Details of the 1 m diurnal tidal range in southern McMurdo Sounds are described by *Goring and Pyne* [2003]. Neither of the two tide gauges in the area was working at the time of the experiment. Instead, tidal model results from the XTide model [*Flater*, 2012] have been used in this study as these results were well correlated with the gauges at times when they were both working concurrently. The experiment commenced after neap tides, ran through the spring tides (∼DOY 301) and once more into neap tides (∼DOY 306) before ending as spring tides returned.

A top-mounted mooring was deployed in 350 m of water, 2.5 km to the SW of the EFC at 77°42.773′ S, 166°21.435′ E, from 20 August through until 7 November 2010. This mooring contained three Aanderaa RCM-9 units coupled with SBE 37 Microcat temperature, salinity, and pressure recorders (Seabird Electronics, USA). The current meter/Microcat pairs were located at depths of 50, 150, and 300 m. The 50 m Microcat stopped recording halfway through the intensive sampling period over days 300–312 but did record the previous 80 days. The current meter at 150 m failed to log data but the Microcat at this depth did work. Upon recovery of the mooring it was found that the line had lifted sufficiently so that the top 10 m had frozen into the growing subice platelet layer. This has been encountered previously on instrument deployments when the buoyancy force from platelet accretion on mooring lines had overwhelmed the mooring ballast (the nature of our remote deployment camp meant we were unable to deploy very heavy ballast blocks).

3. Acoustic Doppler Current Profilers

Data from three acoustic Doppler current profilers (ADCPs) are utilized here; all within 100 m of the sidewall (Table 1). A 75 kHz Teledyne-RDI ADCP and a 600 kHz Aanderaa Recording Doppler Current Profiler (RDCP) were located in one of the containerized laboratories 80 m from the ice wall. A 300 kHz Teledyne-RDI unit was positioned in a second laboratory 35 m from the ice wall, located over the same hydro hole as used for shear microstructure profiling. A magnetic declination offset of 144° was included in all ADCP measurements. Compass testing did not indicate any inconsistencies due to the near-vertical magnetic field. The three acoustic profilers provide a useful spread of scale foci. The 75 kHz unit provides the large-scale, near-full depth perspective, the 300 kHz unit gives a detailed picture of the wake and blocking characteristics of the glacier itself, whilst the 600 kHz unit captures the underice boundary layer structure.

The 2009 pilot study using a 300 kHz ADCP [*Stevens et al.*, 2009] resolved quality data to depths of around 100 m, which is good for a 300 kHz device in these waters. However, during the present work, a number of problems with the ADCP data were encountered, due to the proximity to the glacier; the use of a number of ADCPs in close confines; and the presence of other sampling instruments. For example, the 1.6 m long shear microstructure profiler was apparent in the 75 kHz data. Unlike the 300 kHz data collected in the pilot study [*Stevens et al.*, 2009], this sensor was oriented in such a way that the shear microstructure profiler occasionally registered in one of the beams for a moderate portion of the profile. The bad data were identified using a threshold on the "Percent Good" value returned by the WinADCP sampling software (Teledyne RDI, USA). These data were removed and the gaps, typically of the order of four samples, i.e., 8 min, were

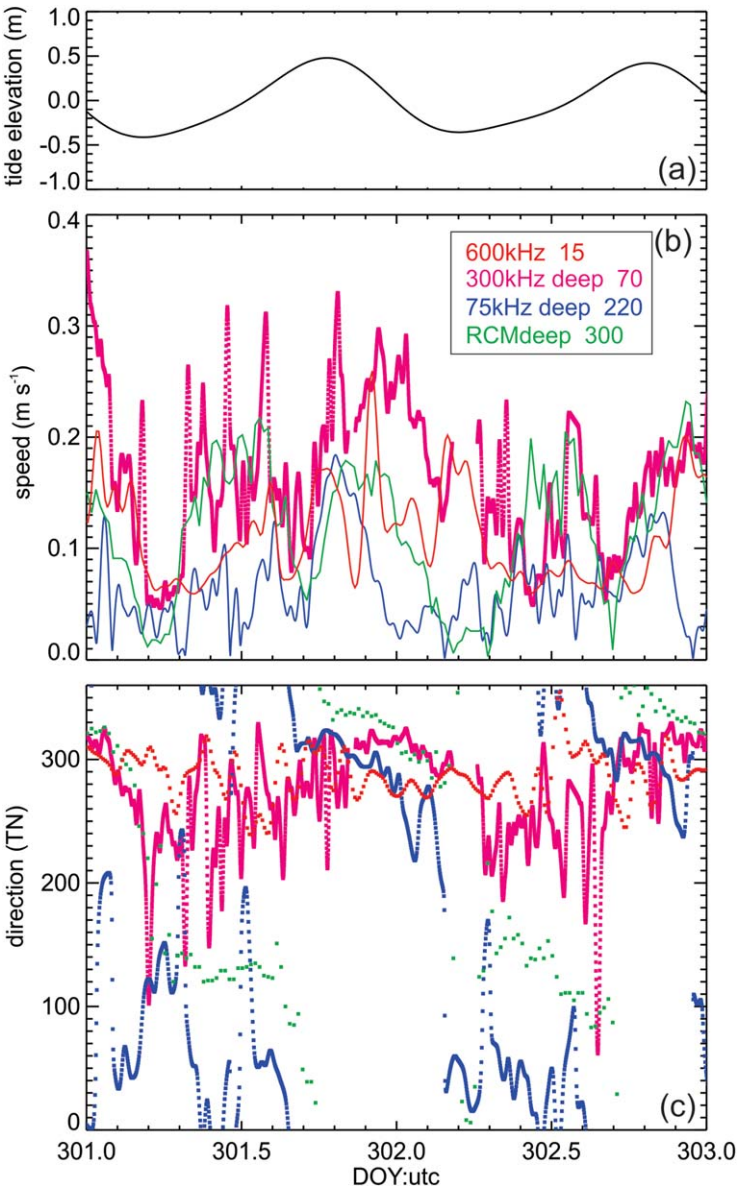

Figure 3. Velocity comparison showing (a) tide, (b) magnitude, and (c) direction for four current records (legend in plot b).

filled by linear interpolation. As a result of the sampling period of the shear profiling, spurious content had a potential 30 min return period in the collected data set.

The 75 kHz ADCP unit was oriented in a way to minimize the likelihood of seeing the glacier wall at depth. So while its deeper data are good, it returned what looked like anomalously low velocities, compared to the higher frequency units, at depths $<$50 m. Despite this, the error velocities were low with an average of only a few cm s^{-1}. Potentially, the 8 m bins were too coarse to capture the detailed layering in the lee of the glacier.

The 300 kHz unit was the closest to the glacier wall so that there is increased potential for sidelobe affects. Also it is possible that the likely small scales of horizontal variability fall within the beam spacing. This reduces the accuracy of the geometric coordinate transformation. Error velocities were at times large with averages typically around 5 cm s^{-1} and individual measures many times this.

A cross comparison of the ADCP data (Figure 3) from the three instruments along with the current meter at the BG mooring (Recording Current Meter (RCM) deep) shows that the flow direction was quite consistent, but that the magnitude was highly variable. The unit closest to the wall, the 300 kHz instrument, returned the highest flows. A merged time series of velocity data was constructed from the 75 and 300 kHz units based on quality control flags derived from backscatter amplitude and error velocity. The two profiles were joined at a depth of 70 m with the merger having a 15 m width either side where there was a reducing proportion of one of the data sets. The majority of the ADCP results presented here will be in the form of this merged data set.

3.1. Profilers

Scalar profiles were recorded using a Seabird Electronics SBE 19+ conductivity-temperature-depth (CTD) profiler. In addition, similar profiles were acquired using a Seabird Electronics (SBE, USA) temperature (SBE 3) and conductivity (SBE 4) sensor pair mounted on the Vertical Microstructure Profiler VMP500 (see below). These VMP-mounted sensors were unpumped so as to not affect the shear data by inducing vibrations. This

meant that the spatial resolution of the salinity was several meters. However, salinity spiking was not particularly apparent due to the very low dynamic range in temperature. Both profilers were kept continuously submerged in between profiles so that the packages maintained equilibrium with the ambient temperature.

Turbulence properties were measured using a Rockland VMP500 (Victoria, Canada) microstructure loose-tethered free-fall profiler with dual shear sensors [*Wolk et al*., 2002]. This enabled estimation of the turbulent energy dissipation rate ε ($m^2\ s^{-3} = W\ kg^{-1}$) using standard techniques [*Wolk et al*., 2002]. This type of device has been used in such conditions previously [*Stevens et al*., 2009, 2011; *Fer et al*., 2012]. Profiles were recorded over a number of periods during the camp occupation. The primary profile data presented here were recorded roughly every 30 min for two 24 h periods located on spring and neap tides. The turbulence profiles often penetrated to 250 m, which was 90 m short of the bed and so do not represent benthic levels of turbulence. In total, 50 km of vertically profiled distance was recorded.

3.2. Turbulence Instrumentation Clusters (TIC)

TIC were deployed at a range of depths from the westernmost site in the field camp (Figure 2c). These sampling packages comprise a 5 MHz acoustic Doppler velocimeter and fast-response temperature and conductivity sensors as described in *McPhee* [2008].

4. Results

4.1. Sea Ice Conditions

At the time of sampling, McMurdo Sound sea ice cover was in retreat after a decade of record coverage due to the presence of large icebergs in the area during the early 2000s [*Robinson and Williams*, 2012]. Pack ice and open water were present off Cape Royds some 20 km north of the sampling locations. Much of the Sound south from this line, down to a little south of the EGT, was first year fast ice. The tip of the EGT was surrounded by 2.3 m thick first year fast ice. There was a residual multiyear ice bridge of ice at least 4 m thick running between the EGT and Big Razorback Island (BRI in Figure 1c).

4.2. Erebus Glacier Tongue

Stevens et al. [2011] assumed a glacier thickness at the wall of around 50 m, based on velocity and stratification structure, as well as the tip thickness identified earlier. However, from the hydrostatic consideration of the freeboard transects, it would appear that the walls of the submerged glacier slopes away gradually so that the center of the glacier, not far back from the tip, is roughly twice this thickness, reaching a depth of 125 m in the middle of the glacier. Furthermore, the repeated GPS transects over the last 1 km of the tongue show that the sidewall complexity is mirrored in the thickness (Figure 2b). An inverted channel forms a cleft so that the plan view lobe at the north-west tip of the glacier is also divided in the vertical. Another 1 km farther toward Ross Island, a large crack on the south side of the tongue was sufficiently open so as to be penetrated by skidoo traveling on the sea ice. This halved the structural width of the EGT and subsequently was the location for the February 2013 calving [*Stevens et al*., 2013].

In addition to surveying the underside of the first year ice, the ROV supplied qualitative but instructive imagery on the condition of the glacier sidewalls (Figure 4). The ice structure appeared uniformly dimpled on a length scale of 10–50 cm at all depths along the wall (Figure 4). Higher on the walls there also appeared to be vertically oriented channels. The imagery also indicated the presence in the water column of both free swimming organisms (most likely amphipods) and suspended ice crystals, both of the order of a few mm in size. Later in the experiment it became clear new ice crystals were forming on the surface of the glacier walls.

4.3. Background Structure and Flows

The background mooring BG (Figures 1c and 2a) to the SW of the EGT tip showed spring tidal speeds reached a maximum of 20 cm s^{-1} and a standard deviation for the entire record of 8 cm s^{-1} (Figure 5). However, rectification and/or background circulation (residual) flows dominated the signal so that at 50 m depth the flow oriented to the NW for the majority the study period had an average speed of 10 cm s^{-1}. The periods where tides dominate do not match exactly the spring tides as there are some springs where the flow does not reverse (e.g., days 280–290 in Figure 5a). In contrast, the data from the deeper current

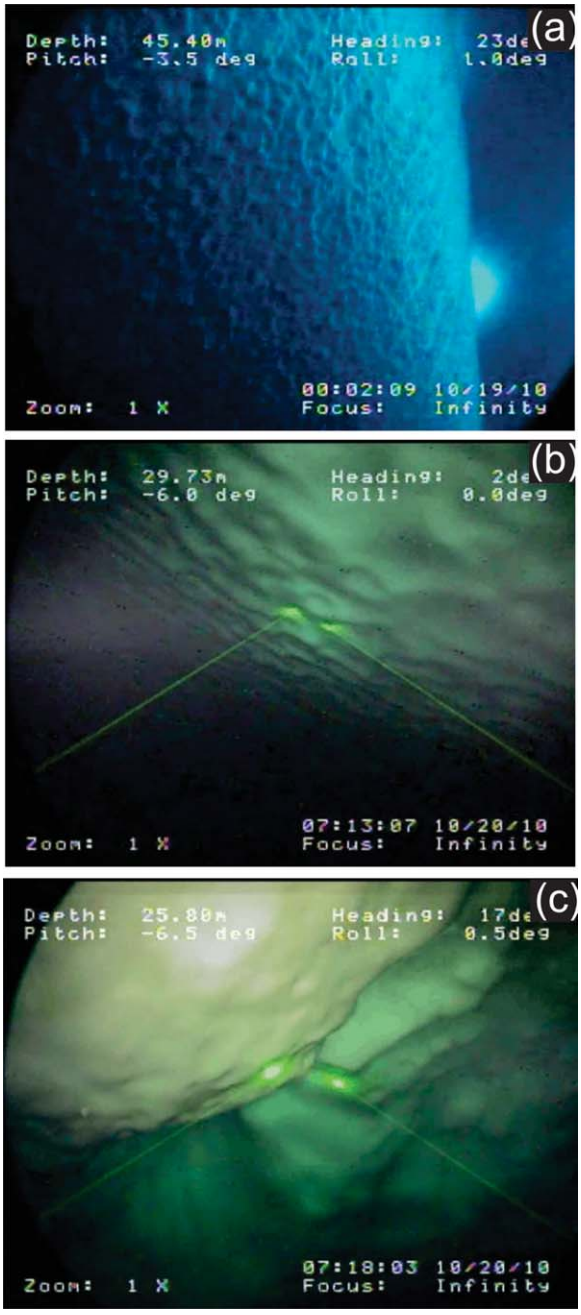

Figure 4. (a) Images from the ROV showing wide view looking diagonally upward from a depth of 45 m where the darker band and bright spot on the right is due to a snow berm and tide crack. (b and c) Details of sidewall at 25–30 m depth shows dimples and indentations, where the laser dots are 40 cm apart.

meter (at 300 m, Figure 5b) contain a bidirectional current (residual of 4 cm s^{-1}, compared to a standard deviation of 8 cm s^{-1}).

The temperature and salinity of the water increased with depth (Figures 5c and 5d). The degree of supercooling in the EGT wake was estimated by shifting the temperature from the 50 m sensor to a hypothetical depth of 25 m and subtracting the freezing temperature at that depth (Figure 5c). This shift from 50 to 25 m, whilst arbitrary, goes some way toward estimating the changes that likely occur downstream of the glacier tongue assuming some eddy recirculation in the vertical behind the obstacle. The fluid at this adjusted position is within 10 mK of local freezing most of the time and crosses the freezing threshold several times for periods of several days, most notably around DOY 260 when the temperature difference stays negative (i.e., supercooled) for 5 days.

The flow was sufficient to generate mooring "knock up" whereby hydrodynamic drag on the mooring caused the mooring to tilt and in doing so, raised the instruments. Consequently, the spring-neap cycle was reflected in the pressure data also. At the same time, near-surface accretion of platelets commenced DOY 260, generating sufficient buoyancy on the line for the mooring to begin to rise, ultimately lifting by a total of 10 m in nearly 2 months (Figure 5e).

4.4. Near-Field Velocity Structure

The full-merged ADCP data set (Figure 6) shows the rectification in the surface waters (i.e., mainly going to west), the relatively low motion at around 130 m, and the persistence of surface currents during the neap tides. Interestingly, the deeper currents (>150 m) do not appear upon the return to spring tides later in the experiment (DOY 306 onward). For spring tides (starting just prior to low tide; Figure 7), the majority of the measured water column was relatively quiescent except the upper ~80 m and the upper 50 m were highly layered. The only exception to this deep quiescence was a deeper flow during the rising phase that was characterized by pulses of accelerated flows beneath 200 m moving to the NE. This was followed by a northwestward period of flow around time 301.8. Upon commencement of the falling tide, the flow uniformly moves toward the NW, but with low flows in the depth range of the deeper half of the glacier's draft (from 90 to 140 m). The largest velocity magnitudes were observed at around 60 m and also at 200 m. The speed deeper in the water column reduced through the falling phase of the tide. The behavior during neap tide was quite different (Figure 8). The only tidally coherent signal is at a depth of 50 m, just beneath the

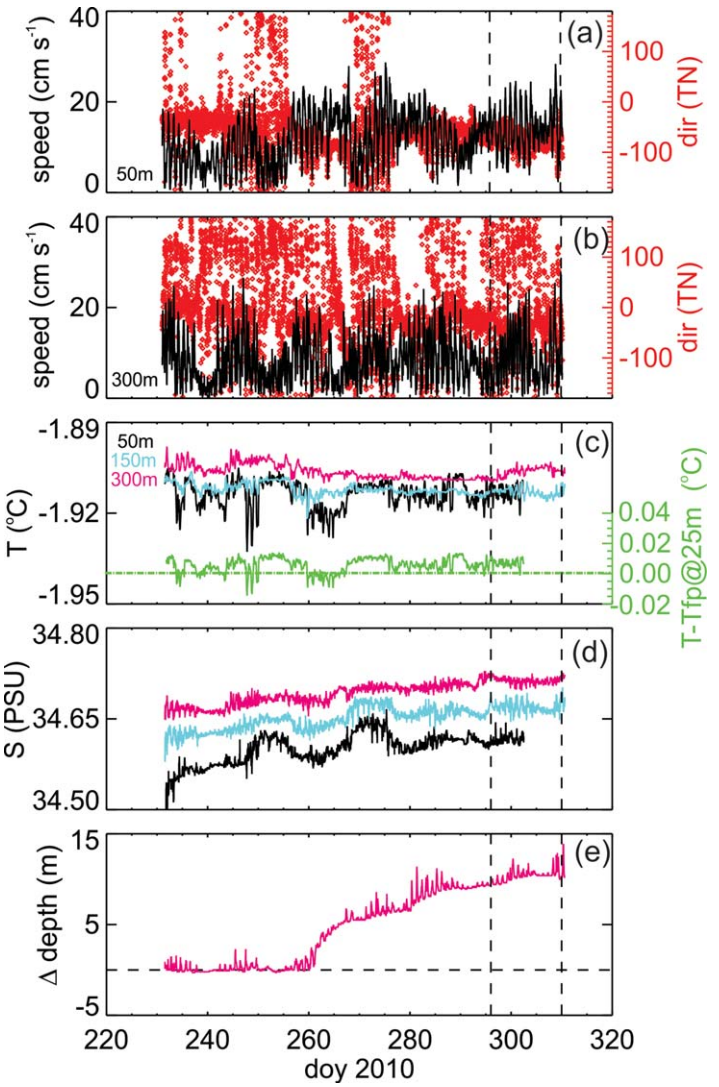

Figure 5. Background (BG) mooring data showing current magnitude and direction at (a) 50 m and (b) 300 m, (c) temperatures at 50, 150, and 300 m, with the difference between 50 m temperature and the freezing point at a nominal depth of 25 m shown at bottom, (d) salinity, and (e) instrument depth change for the deepest sensor at 300 m (positive is upward displacement of instrument). The vertical dashed lines show the period of intense sampling at the EFC.

"near-surface" band seen in Figure 7, which correlates well with the gradient of tidal elevation. Elsewhere the flow is weak.

The uppermost 30 m of near-ice velocity data from the 600 kHz RDCP were characterized by brief periods of high flow, up to 30 cm s^{-1} (Figure 9), and were very much concentrated on westward flow on the falling tide. This matches that seen in the lower frequency ADCP data. The higher vertical resolution and near-ice data from the 600 kHz RDCP indicates that the flow contained a boundary layer type structure (i.e., decaying smoothly to zero at the ice surface) with an *e*-folding depth around 10 m. Other than this the only systematic flow was westward flow very near the surface during the flood (rising) phase. Boundary layer roughness and characterization will be treated in detail elsewhere.

A spectral perspective (Figure 10) of the merged ADCP data with profiler artifacts removed shows that diurnal tides were apparent at most depths, although less so in the range 90–140 m. A weaker signal was also apparent at the inertial/semidiurnal band although it may potentially be a harmonic of the diurnal tide. The profiler-induced artifacts, most likely appearing at ~50 cpd, did not manifest themselves in any obvious way suggesting their removal was successful.

Examples of spectra from specific depths (Figure 10b) indicate that the energy distribution has a slope of roughly f^{-1}. There was no apparent change in energy structure beyond the nominal buoyancy frequency, $N=[(g/\rho_0)\partial\rho/\partial z]^{1/2}$ (g is gravitational acceleration, ρ_0 is a reference density, and $\partial\rho/\partial z$ is the vertical density gradient), although the upper water column did seem to significantly reduce energy rapidly at 40 cpd. Curiously, the shallow band used as an example in Figure 10b has its crest shifted to a moderately higher frequency. This view of the data clearly illustrates that the tidal component is strongest at depth.

4.5. Spatial Structure

The examples of the spatial distribution of current vectors (Figure 11) show remarkable consistency at depth despite the locations being separated by a bathymetric ridge. The TIC velocity data show the flow close to the NW tip of the EGT. The snapshots show regimes whereby there is consistent flow over depth

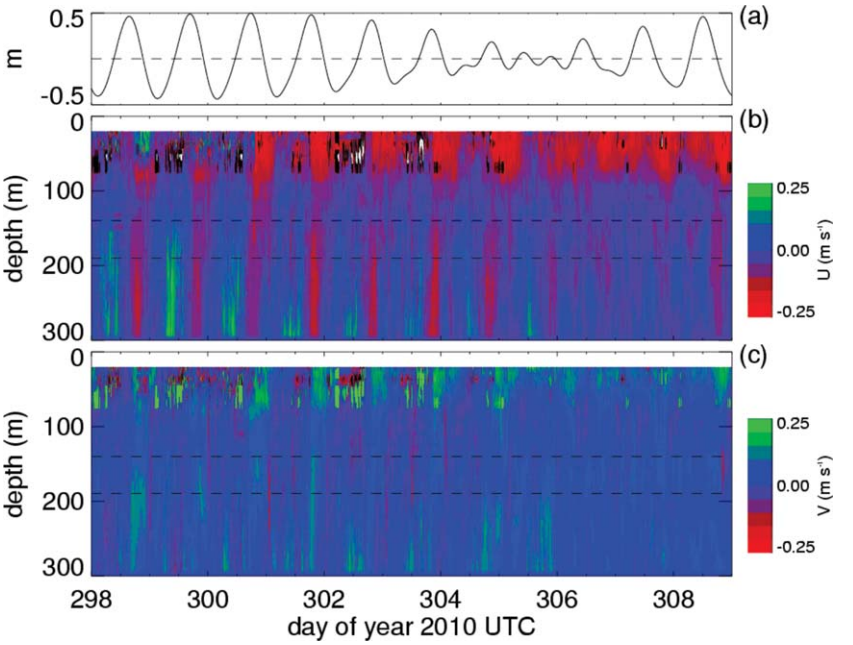

Figure 6. Velocity data from the merging of the 75 and 300 kHz ADCPs showing (a) modeled tidal elevation, (b) u (westward), and (c) v (northward) flows. The upper horizontal dashed line marks the deepest part of the glacier in the vicinity of the sampling whilst the deeper horizontal line marks the crest of the shoal to the west of the glacier tip. The intensive turbulence profiling took place during spring (301) and neap (306) tides.

(Figure 11a), vertical shear (Figure 11b), and relatively quiescent deeper water (Figure 11c). All surface vectors remain constrained within a 60° directional window.

4.6. Stratification

Thermal stratification is typically near its weakest at this time of year [*Mahoney et al.*, 2011] with a range of perhaps only a few 10s of mK (Figures 5 and 12). Salinity stratification is relatively large, however, extending

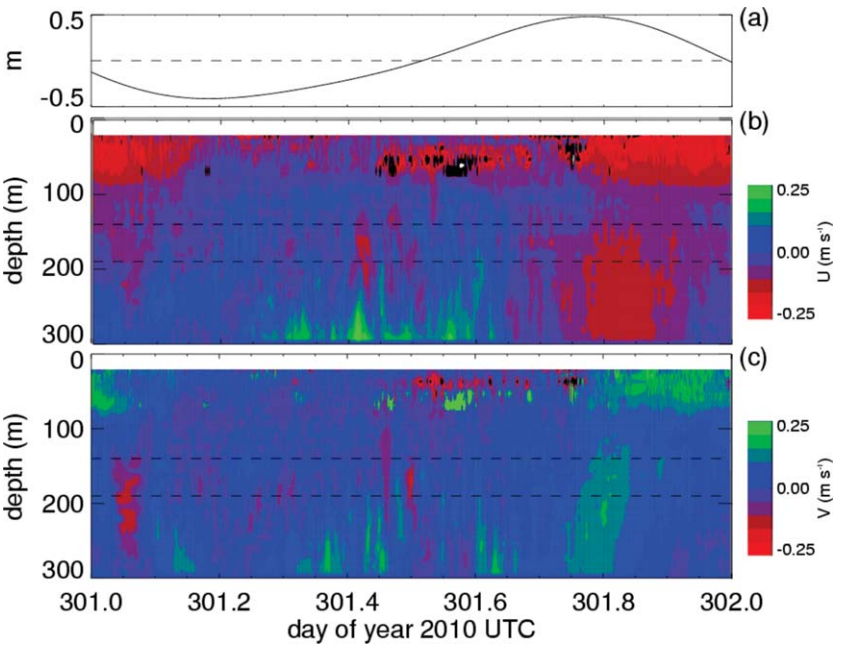

Figure 7. Data from the merging of the 75 and 300 kHz ADCPs for a 24 h section during spring tides showing (a) modeled tidal elevation, (b) u (westward), and (c) v (northward) flows. The horizontal dashed lines are as described in Figure 6.

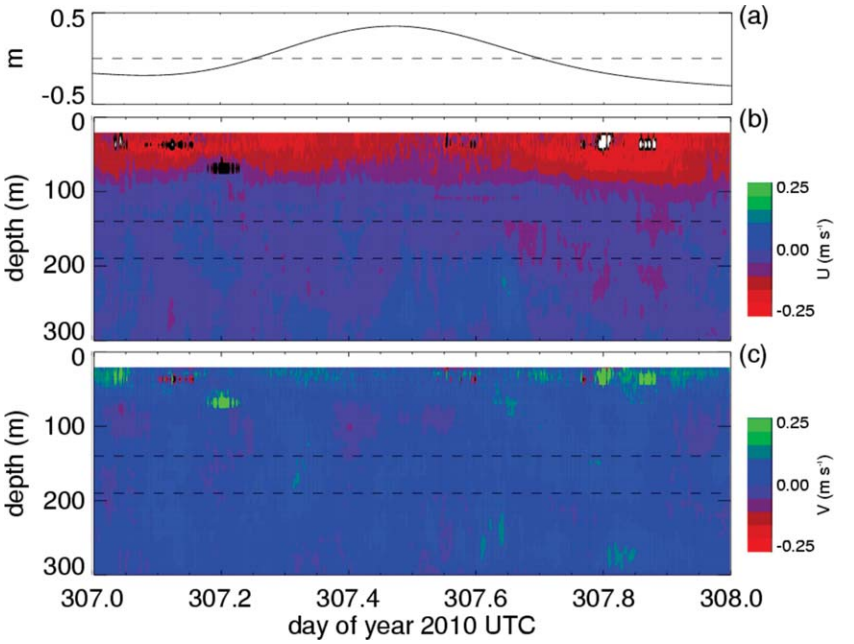

Figure 8. Data from the merging of the 75 and 300 kHz ADCPs for a 24 h section during neap tides showing (a) modeled tidal elevation, (b) u (westward), and (c) v (northward) flows. The horizontal dashed lines are as described in Figure 6.

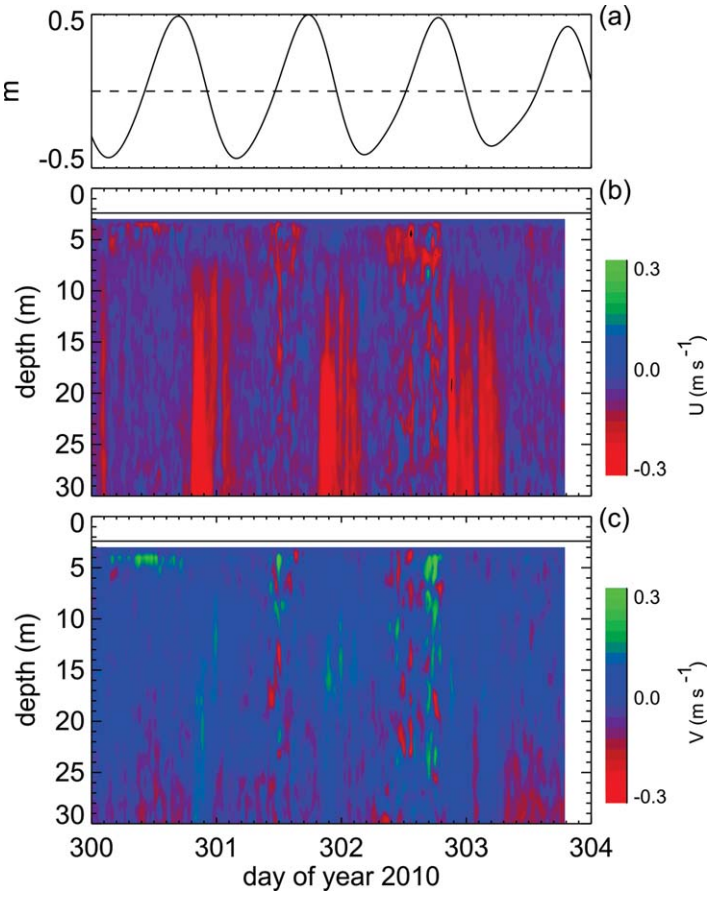

Figure 9. Four day section of (a) modeled tidal elevation data, plus velocity data from the 600 kHz Aanderaa RDCP showing (b) u (eastward) and (c) v (northward).

over 0.2 PSU for the 2010 experiments. There were two clear steps in the example scalar data, at 40 m and a deeper step between 120 and 160 m (Figure 12). This deeper step corresponds to just below the base of the glacier tongue. It is not clear if there was a direct cryospheric effect associated with the shallower step although the ice close by starts to slope away at this depth. Temporal variation in density during the spring tide (Figure 13d) contained substantial vertical structure. This was especially true around the time of maximum ebb flow—right at the point where significant surface layer flow stops, the isopycnal drops by nearly 100 m in the space of around 30 min.

The density structure varies more slowly during neap tide but still with amplitudes exceeding 30 m (Figure 14) and shows a lighter near-surface layer is swept away on

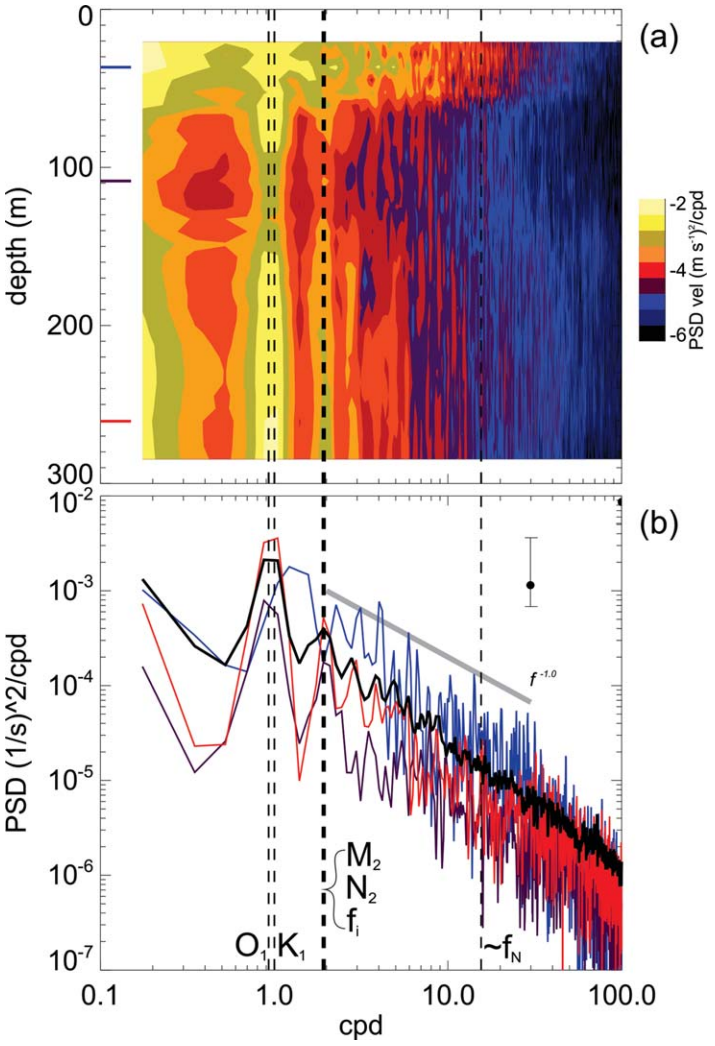

Figure 10. Spectral perspective on merged ADCP velocity data showing (a) velocity power spectral density as a function of depth. From this are excerpted (b) vertical average power spectrum (dark black line) plus three examples from depths of 37, 109, and 270 m. The 95% confidence limit along with tidal frequency components and inertial frequency (f_i) and nominal buoyancy frequency (f_N in cpd) are marked. A slope of cpd^{-1} is shown as a comparison.

the rising tide. Deeper in the water column, the ebb tide brings a pair of rapid depressions in the density structure with isopycnals shifting by ~50 m. The density profiles also provide examples of instability as indicated by the σ_T profile on the left in Figure 12. The influence of small temperature variations at these temperatures has negligible effect on density (i.e., S tracks σ_T very closely). Instability is seen near the surface (top 20 m) in both CTD and microstructure salinity (Figure 12) and deeper (50–150 m) in the water column in the CTD profile. These instabilities will drive turbulent mixing. Overturns can be quantified using the Thorpe scale L_T, a measure of the distance density samples need to be moved in order to provide a monotonic profile [*Galbraith and Kelley*, 1996]. The average overturn scale is 7.6 m for all profiles (Figure 15), but when the overturns are separated based on depth in the water column, the average overturn scale beneath the glacier is actually around 30% larger. There is a slight bias in the present analysis as the upper 10 m or the water column is excluded from the L_T analysis. Furthermore, looking at the spring-neap phase in the tide (Figure 15b), the scale of the overturns during spring tides is more than double that seen during the neap tides. However, recalculating (distributions not shown) for the upper 130 m the average L_T over the spring tides is only 15% greater than the neap equivalent.

4.7. Turbulence

The example microstructure profile (Figure 12) exhibits enhanced mixing at a depth commensurate with the base of the glacier (150 m). Furthermore, the potential temperature was everywhere less than the surface freezing point for the associated salinity. The dissipation rate also increased to its maximum near the underside of the sea ice. During the spring tide sampling, the highest dissipation rates were seen very near the surface early on and then deeper, at around 200 m, later during the rising tide (Figure 13). Structures of increased turbulence coincide with those of increased velocity as there are flows of 25 cm s^{-1} concentrated on 60–80 m depth and then, deeper but variable flows, after DOY 301.3. The dissipation rate matches much of the detailed velocity structure (Figure 7).

The bulk of the higher dissipation rate estimates occurred deeper down during the rising phase of the tide, apparently forced by flow over the ridge running north-south off the tip of the EGT (Figure 2). The vertically

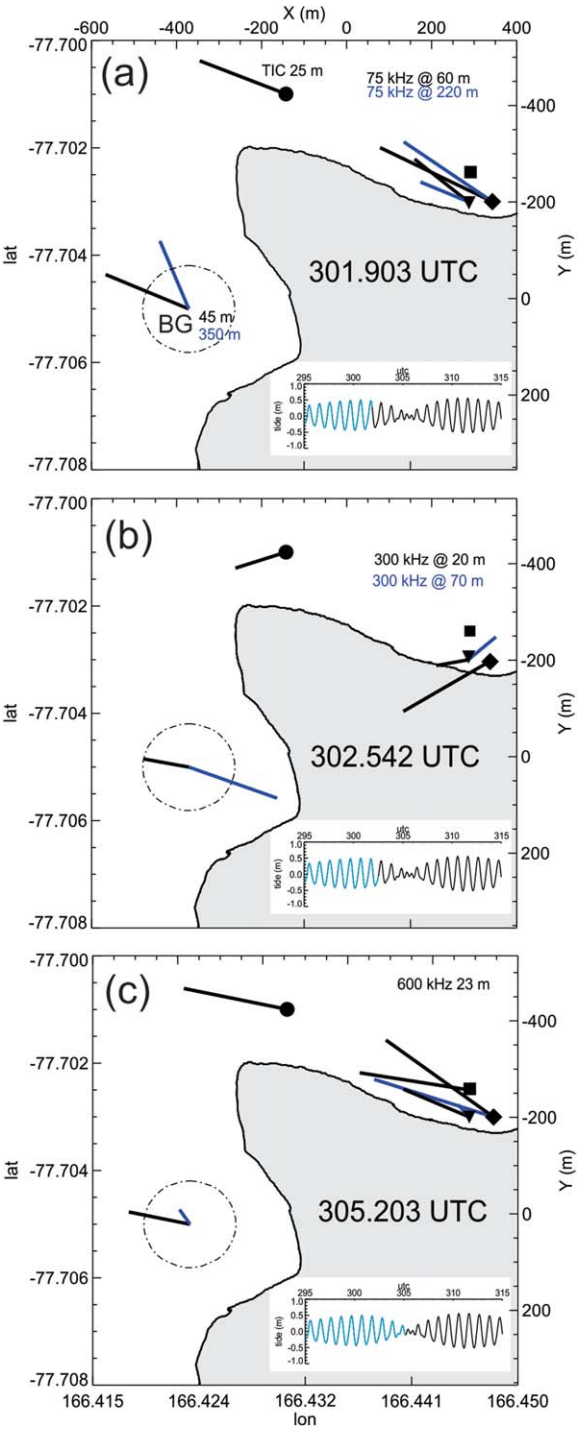

Figure 11. Spatial snapshots showing various current vectors and their orientation relative to the EGT NW tip. The encircled vectors show the BG mooring data but shifted to a position closer to the EGT for clarity (circle diameter is 10 cm s^{-1}). The velocity measurements include 300 kHz (diamond), 75 kHz (triangle), some 600 kHz (square), and the TIC (circle). The black vectors are near surface and the blue vectors are deep. The inset shows the tidal phase so that snapshots are at (a) falling spring tide, (b) rising spring tide, and (c) neap tide.

averaged dissipation rate (Figure 13a) tended to increase from a starting minimum at high tide and peaked just prior to the next high tide. However, when looking at differences through depth the near-surface dissipation rate was greatest on the falling tide (Figure 13) and the enhanced levels appear confined to perhaps only the upper 20 m. During the opposite, rising phase, energy dissipation rates at shallower depths were less structured but nevertheless still reached comparable values of the order of 10^{-6} m^2 s^{-3}.

The depth-averaged dissipation rate (Figure 14a) is more varied during neap tide when compared to spring tide (Figure 13a), with peaks on both rising and falling phases. However, the minimum dissipation rate is again seen at high tide. A bulk view of the turbulent energy dissipation rate is given by collating distributions of observed ε (Figure 16). The overall averaged value of ε is a little under 10^{-7} W kg^{-1}, encompassing individual estimates that range over four decades, although during spring tides a few occurrences of 10^{-5} W kg^{-1} were seen. Bootstrapped 95% confidence intervals (based on 2000 subsampled data sets using 1000 randomly chosen samples) on the spring, neap, and combined distributions are 2.3×10^{-8} m^2 s^{-3} or less.

5. Discussion

5.1. Characterization of the Glacier-Induced Flow Disturbance

An overarching feature of the flow is that a combination of background flow and tidal rectification dominates the flow. Despite this, there is a reasonable tidal influence as seen in the spectral content (Figure 10) and an expectation from measurements elsewhere that tides should dominate [e.g., *Stevens et al.*, 2009, 2011; *Robinson et al.*, 2010]. This suggests that there may be some tidal rectification associated with the islands to the north. Also, it confounded the a priori experimental design that expected that the field camp would be upstream of the glacier for a portion of the study period. A second point is how much of the observed flow and turbulence was focused below the

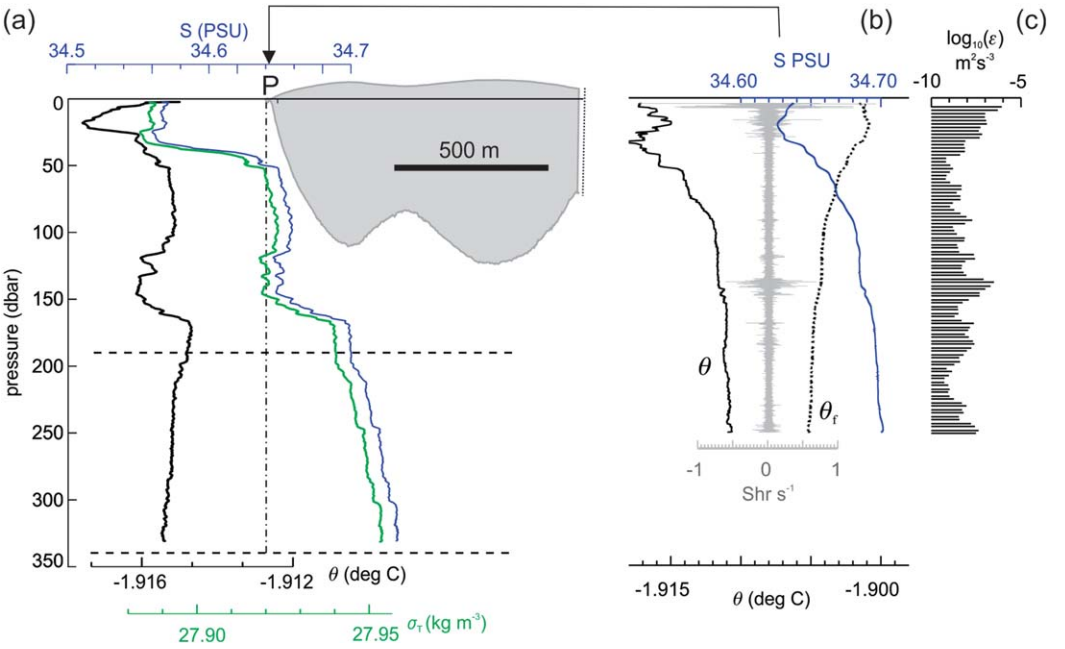

Figure 12. Example of typical profiler results where (a) the gray-shaded area shows the GPS freeboard-derived north-south slice through the glacier (Figure 2—n.b. the survey stopped just short of the southern extent of the glacier and so the truncation is artificial). The profiles of salinity, σ_T, and potential temperature on the left are SBE19+ CTD data recorded at site P (DOY 328.1)—the shear profiler station—going to within 5 m of the bed. The horizontal dashed line is the depth of the ridge near the tip of the EGT (Figure 2) while the lower solid line is the depth of the bed at the profile location. A single microstructure profile (DOY 330.85) included (b) scalar data salinity, potential temperature, as well as velocity shear (Shr), and (c) also energy dissipation rate (the microstructure did not penetrate to the seafloor). The freezing point at the surface pressure θ_f is shown as a dotted line in Figure 12b.

glacier, rather than in its wake region, suggesting that the mixing is at least partly bathymetrically driven. This makes sense when one considers what is known about the bathymetry in the area indicates that a shoal is present right at the tip of the present glacier. The localized influence of bathymetry also suggests that, when considering such systems elsewhere, the variations in depth, which are likely poorly mapped, might be equally important as surface layer obstructions.

In the present data, there are strong changes in flow direction at depths correlating very well with the interfaces seen in Figure 12. There was a persistent westward flow component throughout the depth range of the glacier. The surface layering is curious and was initially thought to be a sampling artifact. A little deeper, at the depth of the base of the glacier, the scalar data (Figure 12) indicate associated overturning structure in density as well as the slightly deeper pycnocline at 170 dbar). These overturns and pycnocline depths can vary in position and strength significantly (e.g., Figure 13d).

The observations reported in *Jacobs et al*. [1981] that initially motivated this work described layering in the stratification and suggested diffusive-convective drivers. However, these layers were not seen in the present sampling. Certainly, the water column is more favorable for diffusive convection during ice-free conditions as seen by *Jacobs et al*. [1981] as this enables greater thermal stratification to develop. However, improved bathymetry since the 1981 study has revealed the shallower region near the tip (minimum depth 190 m) and the clear signature of enhanced turbulence at around this depth. The key profile described in *Jacobs et al*. [1981] was recorded early on 15 Febraury 1979—several days before neap tides so that flows would have been relatively fast. It is at least possible that the layering seen in this profile was generated by shear-driven instability [*Barenblatt et al*., 1993; *Pelegrí and Sangrà*, 1998].

It is challenging to separate the effects of the glacier and the bathymetric variation on the mixing. However, it is possible to look at the changes to a Froude number associated with the two features. The Froude number is given by $Fr = u/(Nh)$ where u and h are nominal flow speed and water depth. With a top-bottom density difference of around 0.05 kg m^{-3}, in the 350 m deep water column (Figure 12), suggests N $\approx$ 0.002

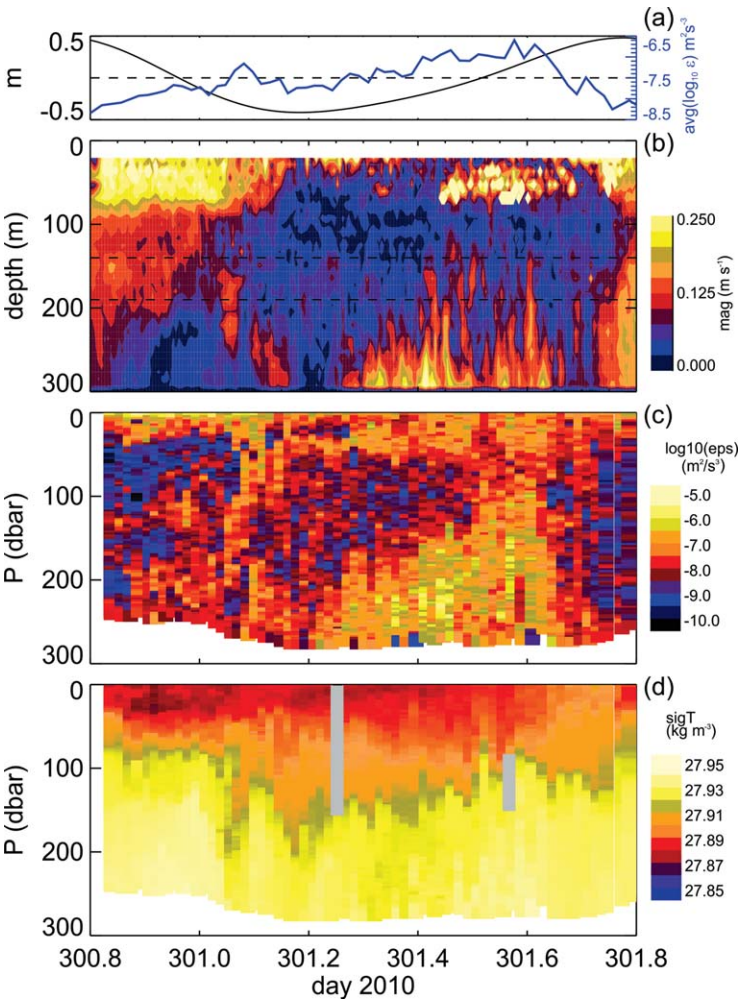

Figure 13. Spring tide turbulence data showing (a) tidal elevation and vertically averaged dissipation rate, (b) velocity magnitude from merged ADCP data set, (c) turbulent energy dissipation rate from VMP turbulence profiler, and (d) potential density from SBE on VMP profiler. Profile sections where the conductivity sensor was contaminated are blanked out gray in the density panel. The horizontal dashed lines are as described in Figure 6.

rad.s^{-1}. Then, for flow speeds of around 0.2 m s^{-1} (at the upper end of the observations from the background mooring) this indicates a subcritical Fr $\approx$ 0.2. However, taking the glacier depth to be 130 m and the shoaling region to be 160 m (i.e., rising to 190 m depth, Figure 12) then these represent 37% and 46% changes in water column depth. Adding one of these obstacles (assuming N remains unchanged) does not raise Fr $>$ 1. However, adding in both results in Fr $>$ 1 and so lee waves and transition to supercritical flow will result [*Dewey et al*., 2005].

Aspects of the present results are quite different from those found in the pilot study in 2009. The current direction from 2009 was more to the NE and the flows were substantially faster. Furthermore, the deeper penetration of the 75 kHz ADCP data (Figures 7 and 8) provides a greatly improved picture compared to that seen in 2009 where the 300 kHz unit only penetrated to depths around 100 m. One of the instruments used in the primary 2010 experiment was exactly that used in the 2009 pilot experiment (the 300 kHz ADCP). Furthermore, the conclusions for the 2010 data range over a number of instruments and locations. The key sampling differences are (i) much shorter period of sampling in 2009 and (ii) a different year with likely different regional drivers.

Despite the differences, there were also similarities between the present work and the pilot study. Again it appears that there was a blocked layer. This layer in the 2010 data is partially removed in the period just after the tidal acceleration ($>$300.6) although it does return at a later time (Figure 6). Additionally, high frequency (20–60 min) oscillations were seen in both field campaigns (Figure 10 shows 2010 data). In the 2010 data, they were most clearly seen beneath the depth of the glacier and during the period of fast eastward flow (300.25–300.6). This is comparable with internal wave observations from close by observed by *Albrecht et al*. [2006] although this study focused on the lower driving frequencies rather than associated high-frequency waves that often accompany internal tides. The variations are at a frequency higher than the local bulk buoyancy frequency (equivalent to around 16 cpd) suggesting that the variations cannot propagate away as free waves and the energy will presumably be contained close by the glacier at least at this time of year. Further to this, as explored by *Albrecht et al*. [2006] and others, the latitude is such that the M_2 tide is comparable to the inertial frequency f_i.

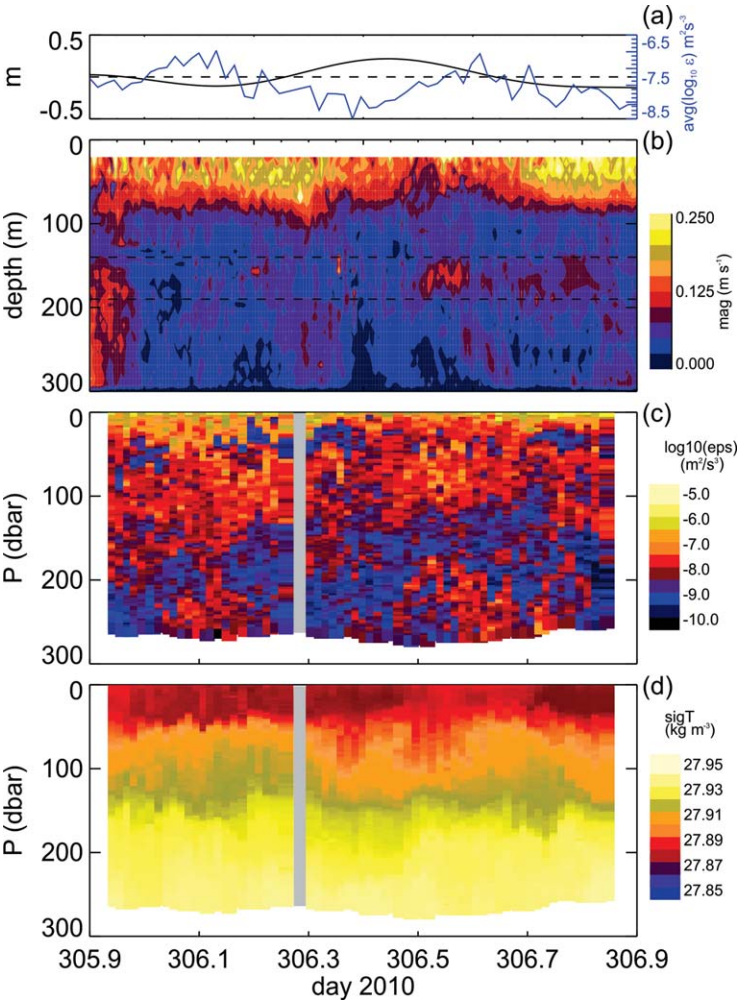

Figure 14. Neap tide turbulence data showing (a) tidal elevation and vertically averaged dissipation rate, (b) velocity magnitude from the merged ADCP data set, (c) turbulent energy dissipation rate from VMP turbulence profiler, and (d) potential density anomaly from SBE on VMP profiler. Missing data are blanked out in gray. The horizontal dashed lines are as described in Figures 6b and 6c.

5.2. Regional Circulation

These data confound the accepted picture of McMurdo Sound regional circulation whereby there is a view that the eastern side of McMurdo Sound is generally southward flowing [*Barry and Dayton*, 1988; *Mahoney et al*., 2011; *Robinson and Williams*, 2012]. Possibly there is some flow separation around Tent Island and we are seeing a return flow. However, the BG mooring should have been outside this envelope, in that it was west of a line between Tent Island and Cape Armitage, but the data collected at this site reveal essentially the same picture as the EFC velocities. The broad scale of the current structure is supported by the observation that the deep BG currents compare well with the deeper 75 kHz data (Figure 3) despite being separated by the ridge at the end of the EGT (Figure 2a).

That said, the appearance of ice shelf water in the region is well documented [*Mahoney et al*., 2011] so it must be viewed that northward flows are occasionally possible and their appearance might reflect very large-scale processes driving the mass balance of the Ross Ice Shelf cavity rather than simply a local phenomenon. *Leonard et al*. [2006] document some northward flow although their results are from a period where icebergs to the north influenced regional circulation [*Robinson and Williams*, 2012; *Dinniman et al*., 2007]. Furthermore, *Holdsworth* [1982] suggests the curvature in the EGT may be the result of northward flow.

Because the Dellbridge Islands to the north act as a strong hydrodynamic barrier, there is little that can be speculated with regard to flow and mixing inshore of the sampled region. Naively, it might be assumed to be quiescent but, as the EGT tip data show, buoyancy can drive substantial flows (i.e., near-surface flow and ε remain significant during neap). This suggests a possible mechanism for enhancing exchange with the innermost parts of the EGT-Erebus Bay and Dellbridge Islands regions.

5.3. Are Local Mixing Rates Elevated and Is There a Spring-Neap Signature?

Local dissipation rates exceed "normal background levels" [*Stevens et al*., 2009]. They do not reach the spring tide level seen in the 2009 pilot study [*Stevens et al*., 2011], but then neither did the flow speed. The mixing beneath the glacier certainly conforms to expectations with elevated mixing correlating with tidal phase. However, the consistently higher near-surface dissipation rate during the neap tide opposes the picture that all the energetics took place during the stronger barotropic forcing period. This will challenge

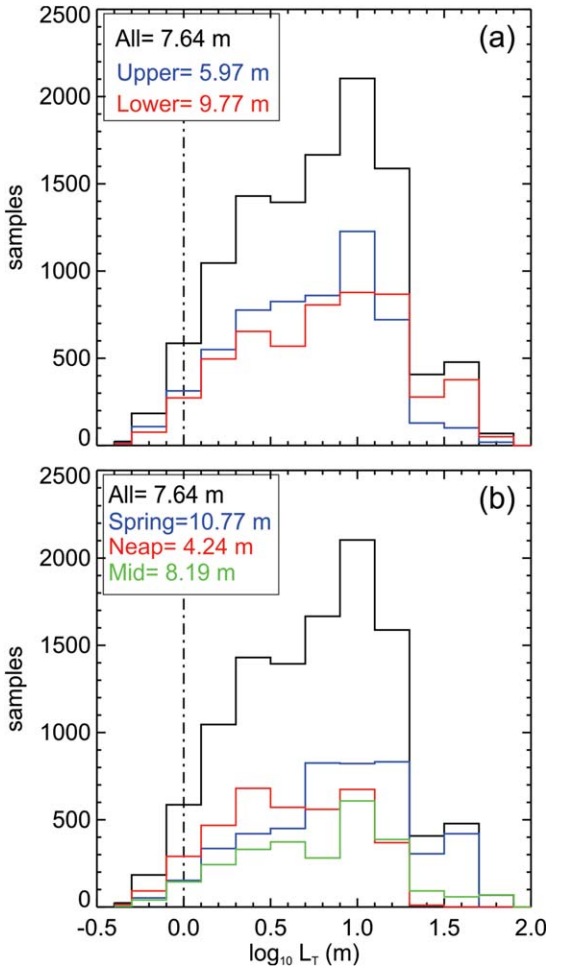

Figure 15. Distributions of Thorpe Scale L_T derived from scalar sensors on the VMP profiler showing separation based on (a) depth in the water column (upper <130 m) and (b) tidal spring-neap phase. In both plots, the total distribution is shown in black. The vertical dashed line at $\log_{10}(L_T) = 0$ (i.e., 1 m) is a cutoff whereby samples to the left are likely unreliable due to sampling limitations.

numerical models to adequately resolve baroclinic processes as well as parameterize buoyancy-induced mixing.

The neap tide turbulence data are interesting in that the strong mixing at large depths was largely absent, although there was some apparent modulation (Figure 14). However, the velocity structure in the 50–100 m band is very clear. What is curious is the strong dissipation rate observed on occasion within 20 m of the surface. Why this should be so on this phase of the tide is not obvious. It could be that the slower flow allows ice crystal growth to develop and remain attached and at the same time inject destabilizing saline fluid at the underice interface.

Considering the dissipation rate distributions (Figure 16), the spring ε distribution is biased to higher values with its average being around 3 times that of the neap value. However, if these averages are recalculated, but only taking dissipation rate values in the top 100 m of the water column (i.e., more directly influenced by the glacier tongue), there is no spring-neap bias and all averages are 10^{-7} W kg^{-1}. These quantities are a factor of 2–3 higher than those seen by *Fer et al*. [2012] adjacent the Brunt Ice Shelf. It is perhaps surprising that the difference is not greater as the flow speeds at the EGT were substantially higher than the Brunt (by as much as a factor of 3, overall).

The study makes for an interesting comparison with the midlatitude flow past a sharp head land situation described by *Edwards et al*. [2004]. These authors did not see strong rectification in their $\pm$0.2 m s^{-1} flows. Instead, they identified and separated barotropic and baroclinic form drag components and estimated dissipation rates (derived from their buoyancy flux data) to be as much as an order of magnitude higher than that seen here. This difference possibly relates to the greater stratification in their study.

By making a number of assumptions it is possible to estimate the energy removed from the regional circulation by the floating component of the glacier. First, the background dissipation rate in the absence of glaciers is assumed to be 10^{-8} W kg^{-1} [*Stevens et al*., 2009]. The glacier-effected dissipation rate is assumed to be an order of magnitude greater, i.e., 10^{-7} W kg^{-1}. Second, the volume over which these elevated dissipation rates occur scales with the tidal excursion so that $V_\varepsilon = LH(\overline{u}T/2)$ where L is glacier length ($\sim$12 km), H is water column depth ($\sim$340 m), T is diurnal period (24 $\times$ 3600 s), and $\overline{u}$ is a representative velocity scale (here picked to be 0.2 m s^{-1}). The volume of influence then is 3.5 $\times$ 10^{10} m^3 suggesting that the rate of energy dissipation due to the glacier is 3.5 MW. Furthermore, there will be a factor of three variations in this energy sink over the spring-neap cycle. *Stevens et al*. [2009] observed integrated dissipation rates of the order of 10 mW m^{-2} around Cape Armitage. Applying this dissipation rate to the area of the EGT (12 km $\times$ 1.5 km) this evaluates to a factor of 20 less than the energy sink due to the EGT described above. As the flow at Cape Armitage is probably the fastest in the region, this suggests that the glacier tongue is a significant (rather than dominant) component of the energy budget of Southern McMurdo Sound.

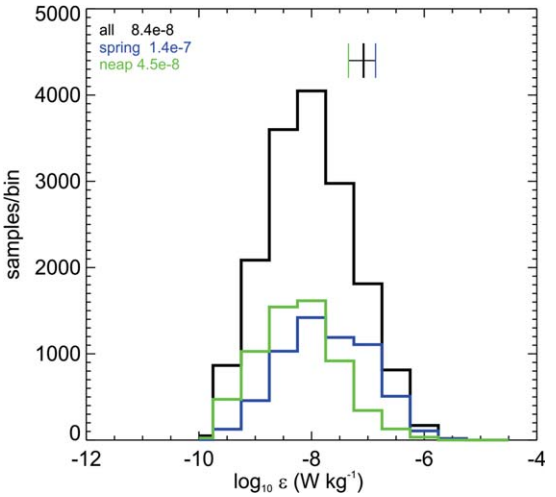

Figure 16. The distribution of the rate of dissipation of turbulent kinetic energy in $\log_{10}(\varepsilon)$ space for all microstructure profiles shown in black. Distributions of dissipation rates for spring and neap tides are also shown in blue and green, respectively. The bars above the histograms show the range of the $\log_{10}$ of the average values.

Further to the energy budget considerations, the increased dissipation rate will drive a comparable increase in vertical diffusion. For example, if a scalar interface might encounter, or be created by, the floating glacier it will subsequently thicken due to the enhanced mixing. The increased dissipation rate results in enhanced vertical diffusion so that the relative thickening of an interface that encounters the glacier mixing increases as the square root of the ratio of near-glacier and background turbulent diffusivities. This will serve to reduce the longevity of supercooled layers as they will be more rapidly mixed with the ambient.

5.4. What Are the Implications for Melting Rate Estimates?

While the focus here is on the glacier-induced influences on the ocean, "basal" melting rates will of course be of interest in terms of regional glaciology. *Holdsworth* [1974] speculated that basal melting of the EGT might exceed 1 m a^{-1}. *Horgan et al*. [2011] estimated the front of the Ross Ice Shelf was melting at around 3 m a^{-1}. *Jenkins et al*. [2010] described basal melting (i.e., basal ablation rate a_b) as a function of water, ice and freezing point temperatures (T_w, T_i, and T_f) as well as boundary layer turbulence parameterized in terms of flow speed ($u_*\Gamma_{(TS)}$), water and ice density (ρ_w and ρ_i), latent heat of fusion (L) and specific heat (c_w, c_i) such that:

$$\rho_i a_b L_i = \rho_i c_i a_b (T_i - T_f) - \rho_w c_w u_* \Gamma_{(TS)} (T_f - T_w).$$

When seeking a_b, the biggest other unknown, the glacier internal temperature, turns out to be relatively unimportant within its likely range (−10 to −20°C). Instead, melting estimates are more strongly influenced by the ocean temperature and the turbulent exchange of heat and salt.

Selecting an ocean temperature of −1.91°C, flow speed of 0.15 m s^{-1}, and a depth of 50 m, the *Jenkins et al*. [2010] approach reveals a melting rate of 1 m a^{-1}. Such bulk estimates encapsulate a range of scales and processes. For example, the ROV imagery shows ∼1 m scale variability (Figure 4b) so that this melting process is nonlinear through the effect on u_*. Consequently, changes in flow speed and or ocean conditions may not be similarly reflected in changes to melt rate. Similar patterns to that seen on the glacier wall, although much more regular, have been observed on the underside of drifting icebergs in both the Antarctic [*Hobson et al*., 2011] and the Arctic [*Forrest et al*., 2012].

Challenges to long-term estimates of the glacier tongue melting relate to adequate spatial estimation—i.e., the sidewalls take up a large proportion of the surface area. Also there are periods of accretion where marine ice grows on the glacier, although *Holdsworth* [1982] indicates that melting is the dominant process. The annual cycles captured by *Leonard et al*. [2006] and *Mahoney et al*. [2011] in two different years suggest that growth might take place for as long as 5 months with the timing of the present observations being just before the initiation of summer warming [*Mahoney et al*., 2011]. Furthermore, as noted above, u_* is likely nonlinear due to the flow interaction with the roughness caused by such accretion as well as the evolution of the structures seen in Figure 4.

The apparent blocking/separation plus the unidirectional flow seen here might have some relationship to *Holdsworth*'s [1982] suggestion that there is greater melting on southern side of EGT, although one might expect constant flow from the south to bring colder or even supercooled water more consistently to the glacier.

5.5. Generalization

Many of the phenomena seen at the EGT must be expected to occur around the Victoria Land coastal glacier tongues. In the circulation paradigm with southward flow on the eastern side of the Sound, rotation should provide a constraining (toward shore) flow, as it would in any northward flowing coastal current off the Victoria Land coast. As noted above, the N-NW-ward flows observed here do not fit the paradigm, so the observations may not be typical. In addition, the Victoria Land glacier tongues are substantially larger than the EGT, with the largest, the Drygalski Ice Tongue, being up to a factor of ~8–10 larger. Hence, tidal excursions become smaller compared to the scale of the glacier itself, which has implications for both tidal drivers of wake mixing as well as local production of supercooled water.

5.6. Summary

Key features from the results include (i) either tidal rectification or a strong regional circulation mean that the tidal flow does not reverse direction. (ii) The combination of the presence of the glacier and bathymetric effects enhances energy dissipation partly in concert with the spring-neap cycle. (iii) However, it appears buoyancy-induced surface flows are important as upper water column mixing is at least as strong during neap tides as spring. The results suggest further exploration of the role played by buoyancy in driving regional circulation is important if the effect on the ocean of such floating topographic features on sea ice and shelf evolution is to be understood.

Acknowledgments

The authors wish to thank Brett Grant, Martin Doble, Jim Stockel, and the staff of Scott Base for their support in the field. Patricia Langhorne, Craig Stewart, Natalie Robinson, Bernard Laval, Robin Robertson, and Michael Williams are thanked for their valuable discussions of the analysis. Andrew Hamilton is thanked for his coordination of the Canadian research component and discussions with Air New Zealand. Joseph Wright assisted in the collection of the GPS data. Satellite imagery is courtesy of NASA. Two anonymous Reviewers are thanked for their comments on an earlier version of this manuscript. Metadata are lodged with Antarctica New Zealand. The work was funded by The New Zealand Royal Society administered Marsden Fund, and US NSF support to Stanton and McPhee. Logistic support was provided by Antarctica New Zealand and travel funding from Air New Zealand.

References

Albrecht, N., R. Vennell, M. Williams, C. Stevens, P. Langhorne, G. Leonard, and T. Haskell (2006), Observation of sub-inertial internal tides in McMurdo Sound, Antarctica, *Geophys. Res. Lett.*, *33*, L24606, doi:10.1029/2006GL027377.

Barenblatt, G. I., M. Bertsch, R. Dal Passo, and V. M. Prostokishin (1993), A mathematical model of turbulent heat and mass transfer in stably stratified shear flow, *J. Fluid Mech.*, *253*, 341–358.

Barry, J. P., and P. K. Dayton (1988), Current patterns in McMurdo Sound, Antarctica and their relationship to local biotic communities, *Polar Biol.*, *8*, 367–376, doi:10.1007/BF00442028.

Debenham, F. (1965), The glacier tongues of McMurdo Sound, *Geogr. J.*, *131*, 369–371.

DeLisle, G., T. Chinn, W. Karlen, and P. Winters (1989), Radio echosounding of Erebus Glacier Tongue, *N. Z. Antarct. Rec.*, *9*, 15–30.

Dewey, R., D. Richmond, and C. Garrett, (2005), Stratified tidal flow over a bump, *J. Phys. Oceanogr.*, *35*, 1911–1927, doi:10.1175/JPO2799.1.

Dinniman, M. S., J. M. Klinck, and W. O. Smith Jr. (2007), Influence of sea ice cover and icebergs on circulation and water mass formation in a numerical circulation model of the Ross Sea, Antarctica, *J. Geophys. Res.*, *112*, C11013, doi:10.1029/2006JC004036.

Dmitrenko, I. A., et al. (2010), Observations of supercooling and frazil ice formation in the Laptev Sea coastal polynya, *J. Geophys. Res.*, *115*, C05015, doi:10.1029/2009JC005798.

Edwards, K., P. MacCready, J. Moum, G. Pawlak, J. Klymak, and A. Perlin (2004), Form drag and mixing due to tidal flow past a sharp point, *J. Phys. Oceanogr.*, *34*, 1297–1312.

Fer, I., K. Makinson, and K. Nicholls (2012), Observations of thermohaline convection adjacent to Brunt Ice Shelf, *J. Phys. Oceanogr.*, *42*,502–508, doi:10.1175/JPO-D-11–0211.1.

Flater, D. (2012), XTide 2.0. [Available at http://www.flaterco.com/xtide.] Accessed on 30 November 2013.

Forrest, A.L., A.K. Hamilton, V. Schmidt, B.E. Laval, D. Mueller, A. Crawford, S. Brucker, and T. Hamilton. (2012). Digital terrain mapping of Petermann Ice Island fragments in the Canadian High Arctic. 21st IAHR International Symposium on Ice: Ice Research for a Sustainable Environment. Dailin, China. 10 pp.

Frezzotti, M. (1997), Ice front fluctuation, iceberg calving flux and mass balance of Victoria Land glaciers, *Antarct. Sci.*, *9*, 61–73.

Galbraith, P. S., and D. E. Kelley (1996), Identifying overturns in CTD profiles, *J. Atmos. Oceanic Technol.*, *13*, 688–702.

Goring, D. G., and A. Pyne (2003), Observations of sea-level variability in Ross Sea, Antarctica, *N. Z. J. Mar. Freshwater Res.*, *37*, 241–249.

Gough, A. J., A. R. Mahoney, P. J. L. Langhorne, M. J. M. Williams, N. J. Robinson, and T. G. Haskell (2012), Signatures of supercooling: McMurdo Sound platelet ice, *J. Glaciol.*, *58*(207), 38–50, doi:10.3189/2012JoG10J218.

Gunn, B. M., and G. Warren (1962), Geology of Victoria Land between the Mawson and Mulock Glaciers, Antarctica, *N. Z. Geol. Surv. Bull.*, *71*, 157 pp.

Hellmer, H. H., F. Kauker, R. Timmermann, J. Determann, and J. Rae (2012), Twenty-first-century warming of a large Antarctic ice-shelf cavity by a redirected coastal current, *Nature*, *485*, 225–228.

Hobson, B. W., A. D. Sherman, and P. R. McGill (2011), Imaging and sampling beneath free-drifting icebergs with a remotely operated vehicle, *Deep Sea Res., Part II*, *58*, 1311–1317, doi:10.1016/j.dsr2.2010.11.006.

Holdsworth, G. (1974), Erebus Glacier Tongue, McMurdo Sound, Antarctica, *J. Glaciol.*, *13*, 27–35.

Holdsworth, G. (1982), Dynamics of Erebus Glacier Tongue, *Ann. Glaciol.*, *3*, 131–137.

Holland, D. M., and A. Jenkins (1999), Modeling thermodynamic ice–ocean interactions at the base of an ice shelf, *J. Phys. Oceanogr.*, *29*, 1787–1800.

Horgan, H. J., R. T. Walker, S. Anandakrishnan, R. B. Alley, (2011). Surface elevation changes at the front of the Ross Ice Shelf: Implications for basal melting, *Journal of Geophysical Research*, *116*, C02005, doi:10.1029/2010JC006192.

Jacobs, S. S., H. E. Huppert, G. Holdsworth, and D. J. Drewry (1981), Thermohaline steps induced by melting of the Erebus Glacier Tongue, *J. Geophys. Res.*, *86*(C7), 6547–6555.

Jenkins, A., K. W. Nicholls, and H. F. J. Corr (2010), Observation and parameterization of ablation at the base of Ronne Ice Shelf, Antarctica, *J. Phys. Oceanogr.*, *40*, 2298–2312, doi:10.1175/2010JPO4317.1.

Leonard, G. H., C. R. Purdie, P. J. Langhorne, T. G. Haskell, M. J. M. Williams, and R. D. Frew (2006), Observations of platelet ice growth and oceanographic conditions during the winter of 2003 in McMurdo Sound, Antarctica, *J. Geophys. Res.*, *111*, C04012, doi:10.1029/2005JC002952.

Mahoney, A. R., A. J. Gough, P. J. Langhorne, N. J., Robinson, C. L. Stevens, M. J. M. Williams, and T. G. Haskell (2011), The seasonal appearance of ice shelf water in coastal Antarctica and its effect on sea ice growth, *J. Geophys. Res.*, *116*, C11032, doi:10.1029/2011JC007060.

McPhee, M. G. (2008), *Air-Ice-Ocean-Interaction: Turbulent Ocean Boundary Layer Exchange Processes*, 215 pp., Springer: New York.

Moffat, C., R. C. Beardsley, B. Owens, and N. van Lipzig (2008), A first description of the Antarctic Peninsula Coastal Current, *Deep Sea Res., Part II*, *55*, 277–293.

Pelegrí, J. L., and P. Sangrà (1998), A mechanism for layer formation in stratified geophysical flows, *J. Geophys. Res.*, *103*(C13), 30,679–30,693, doi:10.1029/98JC01627.

Robinson, N. J., and M. J. M. Williams (2012), Iceberg-induced changes to polynya operation and regional oceanography in the southern Ross Sea, Antarctica, from in situ observations, *Antarct. Sci.*, *24*, 514–526, doi:10.1017/S0954102012000296.

Robinson, N. J., M. J. M. Williams, P. J. Barrett, and A. R. Pyne (2010), Observations of flow and ice-ocean interaction beneath the McMurdo Ice Shelf, Antarctica, *J. Geophys. Res.*, *115*, C03025, doi:10.1029/2008JC005255.

Robinson, W., and T. G. Haskell (1990), Calving of Erebus Glacier Tongue, *Nature*, *346*, 615–616.

Smith, I. J., P. J. Langhorne, T. G. Haskell, H. J. Trodahl, R. D. Frew, and R. M. Vennell (2001), Platelet ice and the land-fast sea ice of McMurdo Sound, Antarctica, *Ann. Glaciol.*, *33*, 21–27.

Stevens, C. L., N. J. Robinson, M. J. M. Williams, and T. G. Haskell (2009), Observations of turbulence beneath sea ice in southern McMurdo Sound, Antarctica, *Ocean Sci.*, *5*, 435–445.

Stevens, C. L., C. L. Stewart, N. J. Robinson, M. J. M. Williams, and T. G. Haskell (2011), Flow and mixing near a glacier tongue: A pilot study, *Ocean Sci.*, *7*, 293–304, doi:10.5194/os-7-293-2011.

Stevens, C. L., P. Sirguey, G. H. Leonard, and T. G. Haskell (2013), Brief communication: The 2013 Erebus Glacier Tongue calving event, *Cryosphere*, *7*, 1333–1337.

Wolk, F., H. Yamazaki, L. Seuront, and R. G. Lueck (2002), A new free-fall profiler for measuring biophysical microstructure, *J. Atmos. Oceanic Technol.*, *19*, 780–793.